ARL-RP-0531 ● AUG 2015

US Army Research Laboratory

A Finite Difference-Augmented Peridynamics Method for Wave Dispersion

by Raymond A Wildman and George A Gazonas

A reprint from International Journal of Fracture. 2014; 190:39-52.

NOTICES

Disclaimers

The findings in this report are not to be construed as an official Department of the Army position unless so designated by other authorized documents.

Citation of manufacturer's or trade names does not constitute an official endorsement or approval of the use thereof.

Destroy this report when it is no longer needed. Do not return it to the originator.

ARL-RP-0531 ● AUG 2015

US Army Research Laboratory

A Finite Difference-Augmented Peridynamics Method for Wave Dispersion

by Raymond A Wildman and George A Gazonas
Weapons and Materials Research Directorate, ARL

A reprint from International Journal of Fracture. 2014; 190:39-52.

REPORT DOCUMENTATION PAGE

Form Approved
OMB No. 0704-0188

1. REPORT DATE *(DD-MM-YYYY)*	2. REPORT TYPE	3. DATES COVERED (From - To)
Aug 2015	Reprint	January 2014 –October 2014

4. TITLE AND SUBTITLE
A Finite Difference-Augmented Peridynamics Method for Wave Dispersion

5a. CONTRACT NUMBER

5b. GRANT NUMBER

5c. PROGRAM ELEMENT NUMBER

6. AUTHOR(S)
Raymond A Wildman and George A Gazonas

5d. PROJECT NUMBER

5e. TASK NUMBER

5f. WORK UNIT NUMBER

7. PERFORMING ORGANIZATION NAME(S) AND ADDRESS(ES)
US Army Research Laboratory
ATTN: RDRL-WMM-B
Aberdeen Proving Ground, MD 21005-5069

8. PERFORMING ORGANIZATION REPORT NUMBER
ARL-RP-0531

9. SPONSORING/MONITORING AGENCY NAME(S) AND ADDRESS(ES)

10. SPONSOR/MONITOR'S ACRONYM(S)

11. SPONSOR/MONITOR'S REPORT NUMBER(S)

12. DISTRIBUTION/AVAILABILITY STATEMENT
Approved for public release; distribution unlimited.

13. SUPPLEMENTARY NOTES
A reprint from International Journal of Fracture. 2014; 190:39-52.

14. ABSTRACT
A method is presented for the modeling of brittle elastic fracture which combines peridynamics and a finite difference method to mitigate the wave dispersion properties of peridynamics. Essentially, a finite difference method is used in the bulk for wave propagation modeling, while peridynamics is automatically inserted in high strain areas to model crack initiation and growth. The dispersion properties of finite difference methods and discretized peridynamics are reviewed and the interface reflection properties between the two regions are investigated. Results show that the augmented method can improve the modeling of wave propagation and boundary conditions. In addition, the numerical stress intensity factor computed at a crack tip shows reduced oscillations in the augmented method, likely due to the improved dispersion properties of the bulk. Dynamic fracture simulations show a difference in crack paths between the methods.

15. SUBJECT TERMS
Finite difference; peridynamics; fracture; wave propagation

16. SECURITY CLASSIFICATION OF:			17. LIMITATION OF ABSTRACT	18. NUMBER OF PAGES	19a. NAME OF RESPONSIBLE PERSON
a. REPORT	b. ABSTRACT	c. THIS PAGE			Raymond A Wildman
Unclassified	Unclassified	Unclassified	UU	20	19b. TELEPHONE NUMBER (Include area code) 410-306-2232

Int J Fract (2014) 190:39–52
DOI 10.1007/s10704-014-9973-1

ORIGINAL PAPER

A finite difference-augmented peridynamics method for reducing wave dispersion

Raymond A. Wildman · George A. Gazonas

Received: 9 July 2014 / Accepted: 7 October 2014 / Published online: 21 October 2014

Abstract A method is presented for the modeling of brittle elastic fracture which combines peridynamics and a finite difference method to mitigate the wave dispersion properties of peridynamics. Essentially, a finite difference method is used in the bulk for wave propagation modeling, while peridynamics is automatically inserted in high strain areas to model crack initiation and growth. The dispersion properties of finite difference methods and discretized peridynamics are reviewed and the interface reflection properties between the two regions are investigated. Results show that the augmented method can improve the modeling of wave propagation and boundary conditions. In addition, the numerical stress intensity factor computed at a crack tip shows reduced oscillations in the augmented method, likely due to the improved dispersion properties of the bulk. Dynamic fracture simulations show a difference in crack paths between the methods.

Keywords Finite difference · Peridynamics · Fracture · Wave propagation

1 Introduction

Computational mechanics problems involving the fracture and failure of materials are difficult to solve using partial differential equation formulations as any discontinuity introduced by such failure causes difficulties in both the computation and formulation. Peridynamics proposes to address this issue by replacing the spatial differential operators in the standard continuum mechanics equations with integral operators that converge to those differential operators under certain conditions (Silling 2000; Silling et al. 2007; Emmrich and Weckner 2006). When discretized and coupled with a damage model, peridynamics has been shown to be capable of matching a number of experimental results in both brittle and ductile fracture problems (Silling and Askari 2005; Ha and Bobaru 2010, 2011; Wildman and Gazonas 2013; Foster et al. 2010). In addition, peridynamics has been applied to other fields of physics, such as heat transfer (Bobaru and Duangpanya 2010) and electromigration (Gerstle et al. 2008). While peridynamics has seen success in matching fracture patterns observed in experiments, issues remain, such as its behavior at material boundaries and its dispersion characteristics (Weckner and Abeyaratne 2005; Mikata 2012). Here, we attempt to address dispersion in peridynamic simulations by coupling with a finite difference solver to compute internal forces.

Finite difference methods have a long history, beginning with a proof of their stability properties for hyperbolic partial differential equations (Courant et al. 1928) and similar methods exist in many fields; a short list includes electromagnetics (Alterman and Karal 1968; Zahradnik and Hron 1992), elasticity (Yee 1966; Taflove and Brodwin 1975), and diffusion (Brian 1961).

R. A. Wildman (✉) · G. A. Gazonas
U.S. Army Research Laboratory, Attn: RDRL-WMM-B, US Army Research Laboratory, Aberdeen, MD 21005, USA
e-mail: raymond.a.wildman.civ@mail.mil

Their first implementations relied on rectangular, uniform grids, though finite difference methods have been developed for unstructured grids and curved regions (Hesthaven and Warburton 2002).

A finite difference method (FDM) will be augmented with peridynamics in this work, as the most basic implementations of FD methods are point-based on uniform grids, much like standard peridynamic discretizations. The compatibility of the spatial discretization allows for straightforward switching between the two methodologies. Essentially, all that changes between the two formulations is the calculation of internal forces: in FD methods, an approximation of the divergence of the stress tensor is used, and in peridynamics, the integral of a micro-force function is used over some finite horizon. In fact, peridynamics can be viewed as a sum of continuous differences, and when discretized appears much like a weighted sum of finite differences. In addition, peridynamics is known to be less accurate on boundaries so the finite difference discretization can be used to implement boundary conditions in undamaged regions.

Adaptive methods for peridynamics have been introduced to improve its accuracy (Bobaru et al. 2009; Bobaru and Ha 2011). These methods use an adaptive grid to refine the solution around crack tips and other stress concentrations. It has been shown that peridynamics is more accurate and converges to the continuum mechanics formulation as the horizon shrinks. Of course, a shrinking horizon must be coupled with a refined grid, hence the adaptive refinement method. Here, we attempt to gain more accurate wave propagation using a different formulation in the bulk, rather than adaptive refinement. As will be shown, a more accurate dispersion relation leads to more accurate stress concentrations around crack tips than peridynamics alone, without the need for adaptive refinement.

Currently, hybrid peridynamics/finite element methods have been developed (Lubineau et al. 2012; Azdoud et al. 2013, 2014). The combination of peridynamics with a local finite element method has the same goal as this work, though current literature is restricted to quasi-static problems and the method requires the local and non-local regions be set *a priori*. In addition, Seleson et al. (2013) describe a hybrid finite difference/peridynamics model using a blending function in 1D, though again, the focus is on preset, unchanging local/nonlocal regions. In contrast, this work will focus on the dynamic insertion of peridynamic nodes into a finite difference domain. Previous approaches have used blending functions to ease the reflections from these disparate computational domains, though here the focus will be on dynamic insertion.

The remainder of the paper proceeds as follows: In Sect. 2, peridynamics is summarized and a specific finite difference method is formulated. In addition, the dispersion properties of both discretizations are reviewed, and finally a hybrid approach is detailed. In Sect. 3, numerical results are given, including a demonstration of the dispersion properties of both methods, interface reflections between the two computational regions, a comparison of stress intensity factors at a stationary crack tip, and finally a dynamic crack propagation problem. Section 4 concludes the paper.

2 Formulation

In this section, first peridynamics and FDM are summarized, followed by a discussion of their numerical dispersion properties. Subsequently, a hybrid method is presented, which essentially uses finite difference approximations on discretization nodes undergoing small strain, and peridynamics in areas of high strain.

2.1 Peridynamics

To facilitate comparisons of dispersion characteristics, the peridynamics formulation is the linearization of the standard bond-based method described in (Silling 2000). Bond-based peridynamics can be stated as the integro-differential relation

$$\rho \frac{\partial^2}{\partial t^2}\mathbf{u} = \int_{\mathcal{H}_\mathbf{x}} \mathbf{f}\left(\mathbf{u}' - \mathbf{u}, \mathbf{x}' - \mathbf{x}\right) d\mathbf{x}' + \mathbf{b}, \tag{1}$$

where bold type indicates a vector, $\mathbf{u} = \mathbf{u}(\mathbf{x}, t)$, $\mathbf{u}' = \mathbf{u}\left(\mathbf{x}', t\right)$, ρ is the density (assumed to be homogeneous), $\mathcal{H}_\mathbf{x}$ is the horizon or region of influence at point $\mathbf{x}$ and is typically a sphere of radius δ, $\mathbf{b}$ is a body force, and $\mathbf{f}$ is a peridynamic force function. The linearized version of Eq. (1) can then be stated as

$$\rho \frac{\partial^2}{\partial t^2}\mathbf{u} = \int_{\mathcal{H}_\mathbf{x}} c\frac{\boldsymbol{\xi} \otimes \boldsymbol{\xi}}{|\boldsymbol{\xi}|^3}\boldsymbol{\eta} d\mathbf{x}' + \mathbf{b}, \tag{2}$$

where $\boldsymbol{\xi} = \mathbf{x}' - \mathbf{x}$, $\boldsymbol{\eta} = \mathbf{u}' - \mathbf{u}$ and c is a material constant that can be related to classical elasticity constitutive

parameters. For example, in 3D, c is related to Young's modulus E and Poisson's ratio ν as

$$c = \frac{6E}{\pi\delta^4(1-2\nu)} \tag{3}$$

where $\nu = 1/4$, in 2D plane stress we have

$$c = \frac{6E}{\pi\delta^3(1-\nu)}, \tag{4}$$

where $\nu = 1/3$ and in 2D plane strain we have

$$c = \frac{6\lambda}{\pi\delta^3\nu}, \tag{5}$$

where $\nu = 1/4$ and λ is Lamé's first parameter, all of which are derived via matching the elastic strain energy of the classical and peridynamic formulations (Ha and Bobaru 2010).

A standard, point-based discretization of Eq. (2), is used and is given by

$$\rho\frac{\partial^2}{\partial t^2}\mathbf{u}_m = \sum_{n=1}^{N_m} c\frac{\boldsymbol{\xi}_{mn}\otimes\boldsymbol{\xi}_{mn}}{|\boldsymbol{\xi}_{mn}|^3}\boldsymbol{\eta}_{mn}V_{mn} + \mathbf{b}_m, \tag{6}$$

where N_m is the number of nodes in the horizon $\mathcal{H}_{\mathbf{x}}$ of node $\mathbf{x}_m$, $\boldsymbol{\xi}_{mn} = \mathbf{x}_n - \mathbf{x}_m$, $\boldsymbol{\eta}_{mn} = \mathbf{u}(\mathbf{x}_n, t) - \mathbf{u}(\mathbf{x}_m, t)$, and V_{mn} is the volume (or area in 2D) of the n^{th} node associated with node m (Silling and Askari 2005). This distinction on the volume is necessary because exact integration weights that account for the edge of the horizon are used. In other words, the regions or cells associated with nodes in the reference configuration are assumed to be rectangular (with sides given by the discretization sizes Δx and Δy), and if the entire rectangle resides within a node's horizon then its area is simply the area of the square (in 2D). If the region intersects the horizon, then its partial area is computed exactly by using the divergence theorem to convert the area integral into a line integral that encloses the integration region. The line integral will then be a collection of zero or more straight line segments and a circular arc, all of which can be computed exactly.

The temporal discretization is a velocity Verlet method, stated as

$$\begin{aligned}
\mathbf{v}^{k+1/2} &= \mathbf{v}^k + \frac{\Delta t}{2}\mathbf{a}^k,\\
\mathbf{u}^{k+1} &= \mathbf{u}^k + \Delta t\mathbf{v}^{k+1/2},\\
\mathbf{a}^{k+1} &= \frac{(\mathbf{F}+\mathbf{b})}{\rho},\\
\mathbf{v}^{k+1} &= \mathbf{v}^{k+1/2} + \frac{\Delta t}{2}\mathbf{a}^{k+1},
\end{aligned} \tag{7}$$

where $\mathbf{a} = \partial^2\mathbf{u}/\partial t^2$ is the acceleration, $\mathbf{v} = \partial\mathbf{u}/\partial t$ is the velocity, $\mathbf{F}$ is the internal force given as the first term of the right hand side of Eq. (6), $\mathbf{b}$ is a given body force (that can also be used to apply boundary loads), and Δt is the time step size.

Most importantly, peridynamics implements material failure by separating "bonds," i.e. removing nodes from a given node's horizon so that they do not interact. The simplest damage model in the literature is to remove a bond based on a bond strain measure, the linearized version of which is given as

$$s_{mn} = \frac{\boldsymbol{\eta}_{mn}\cdot\boldsymbol{\xi}_{mn}}{|\boldsymbol{\xi}_{mn}|^2}, \tag{8}$$

with the definitions of $\boldsymbol{\xi}_{mn}$ and $\boldsymbol{\eta}_{mn}$ given above. A maximum strain can be given as a constant, giving the failure criterion

$$s_{mn} > s_{\max}, \tag{9}$$

where $s_{\max}$ is a maximal bond strain, typically given in terms of a fracture energy as

$$s_{\max} = \sqrt{\frac{4\pi G_0}{9E\delta}}, \tag{10}$$

where G_0 is an energy release rate (Silling and Askari 2005). If Eq. (9) is met for a given bond pair $\{m, n\}$, node n is removed from node m's family (and vice versa), and not included in the summation of Eq. (6). After a bond breaks, its supported load is transferred to other bonds in the nodes' families, encouraging more bond breakage and leading to progressive crack formation.

While peridynamics provides a description of the elastic wave equation that is accurate under a converging horizon and its discretized form gives a useful damage model, in general its dispersion characteristics are not consistent with a linear elastic material. Other numerical methods can provide more accurate wave propagation modeling and augment peridynamics' superior handling of discontinuities.

2.2 Finite difference method

A finite difference formulation follows standard elasticity theory and discretizes its differential operators with finite difference stencils. The linear elastic wave equation can be stated as

$$\rho\frac{\partial^2}{\partial t^2}\mathbf{u} = \nabla\cdot\overline{\boldsymbol{\sigma}} + \mathbf{b}, \tag{11}$$

where bold type with an overbar represents a second-rank tensor, **b** is a body force, the stress, $\overline{\boldsymbol{\sigma}}$ is given by

$$\overline{\boldsymbol{\sigma}} = \overline{\overline{\mathbf{C}}} : \overline{\boldsymbol{\epsilon}} = \overline{\overline{\mathbf{C}}} : \frac{1}{2} \left(\nabla \mathbf{u} + \mathbf{u} \nabla \right), \tag{12}$$

two overbars represent a fourth-rank tensor, and $\overline{\overline{\mathbf{C}}}$ is a fourth-rank constitutive tensor. In 3D, the isotropic, linear elastic constitutive tensor is given by

$$\overline{\overline{\mathbf{C}}} = \begin{bmatrix} 2\mu+\lambda & \lambda & \lambda & 0 & 0 & 0 \\ \lambda & 2\mu+\lambda & \lambda & 0 & 0 & 0 \\ \lambda & \lambda & 2\mu+\lambda & 0 & 0 & 0 \\ 0 & 0 & 0 & 2\mu & 0 & 0 \\ 0 & 0 & 0 & 0 & 2\mu & 0 \\ 0 & 0 & 0 & 0 & 0 & 2\mu \end{bmatrix}, \tag{13}$$

where the Lamé parameters λ and μ are

$$\lambda = \frac{E\nu}{(1+\nu)(1-2\nu)}, \tag{14}$$

and

$$\mu = \frac{E}{2(1+\nu)}. \tag{15}$$

Now, the above set of equations can be specialized with the restrictions on Poisson's ratio inherent in peridynamics. For example, for 2D plane strain the constitutive tensor becomes

$$\overline{\overline{\mathbf{C}}} = \frac{2}{5} E \begin{bmatrix} 3 & 1 & 0 \\ 1 & 3 & 0 \\ 0 & 0 & 2 \end{bmatrix}, \tag{16}$$

resulting in the coupled equations

$$\begin{aligned} \rho \frac{\partial^2}{\partial t^2} u_{\mathrm{x}} &= \frac{2}{5} E \left(3 \frac{\partial^2}{\partial x^2} u_{\mathrm{x}} + 2 \frac{\partial^2}{\partial x \partial y} u_{\mathrm{y}} + \frac{\partial^2}{\partial y^2} u_{\mathrm{x}} \right) + b_{\mathrm{x}}, \\ \rho \frac{\partial^2}{\partial t^2} u_{\mathrm{y}} &= \frac{2}{5} E \left(3 \frac{\partial^2}{\partial y^2} u_{\mathrm{y}} + 2 \frac{\partial^2}{\partial x \partial y} u_{\mathrm{x}} + \frac{\partial^2}{\partial x^2} u_{\mathrm{y}} \right) + b_{\mathrm{y}}. \end{aligned} \tag{17}$$

The remaining two formulations follow similarly, for example, the plane stress formulation is identical but with the factor of $2/5E$ replaced with $3/8E$.

Often, finite difference discretizations for elasticity will use two or four staggered grids, solving for the displacement on one grid and the stress on the second, or different components of each on four grids (Virieux 1986). (This approach is known as the Yee cell in electromagnetics (Yee 1966).) Though staggered grid approaches can be more accurate, here we use a single grid to ensure compatibility with the peridynamics grid. (In an extension of this method, state-based peridynamics could be implemented in a dual, staggered-grid discretization with the more standard finite difference formulation.) Rather, the second order spatial derivatives will be discretized with a standard central difference approximation given as:

$$\begin{aligned} &\frac{\partial^2}{\partial x^2} f(x,y) \\ &\quad \approx \frac{f(x+\Delta x, y) - 2f(x,y) + f(x-\Delta x, y)}{\Delta x^2}, \end{aligned} \tag{18}$$

$$\begin{aligned} &\frac{\partial^2}{\partial y^2} f(x,y) \\ &\quad \approx \frac{f(x, y+\Delta y) - 2f(x,y) + f(x, y-\Delta y)}{\Delta y^2}, \end{aligned} \tag{19}$$

and

$$\begin{aligned} \frac{\partial^2}{\partial x \partial y} f(x,y) \approx & \frac{f(x+\Delta x, y+\Delta y)}{\Delta x \Delta y} \\ & - \frac{f(x+\Delta x, y-\Delta y)}{\Delta x \Delta y} \\ & + \frac{f(x-\Delta x, y-\Delta y)}{\Delta x \Delta y} \\ & - \frac{f(x-\Delta x, y+\Delta y)}{\Delta x \Delta y}, \end{aligned} \tag{20}$$

where Δx and Δy are the discretization sizes in x and y respectively. The temporal discretization is again the velocity Verlet method shown in Eq. (7).

2.3 Numerical dispersion

Next, we discuss the numerical dispersion inherent in both peridynamics and FDM, as any interface between the two methods with different dispersion characteristics will result in wave reflections. Previous work has shown that the peridynamics formulation displays dispersion, even before discretization (Weckner and Abeyaratne 2005) and it is well known that FDM suffers from numerical dispersion. In 1D, the linearized form of peridynamics behaves as a continuous sum of differences, much like discretized finite difference methods. For example, specializing Eqs. 2 and 6 to 1D gives

$$\rho \frac{\partial^2}{\partial t^2} u = \int_{\mathcal{H}_x} c \frac{u' - u}{|x' - x|} dx', \tag{21}$$

which can be discretized as

$$\rho \frac{\partial^2}{\partial t^2} u_m = \sum_{n=1}^{N_m} c \frac{u_n - u_m}{|x_n - x_m|} V_{mn}. \tag{22}$$

A central difference scheme can be recovered by setting the horizon to be equal to the spatial discretization size $\delta = \Delta x$, resulting in $V_{mn} = \Delta x$, $N_m = 2$ (the two nodes adjacent to node m), $c = E/\delta^2$, and giving

$$\sum_{\substack{n=-1 \\ n \neq 0}}^{1} \frac{E}{\delta^2} \frac{u_n - u_m}{|x_n - x_m|} \Delta x = E \frac{u_{m-1} - 2u_m + u_{m+1}}{\Delta x^2}. \tag{23}$$

A standard discretization of 1D peridynamics with a horizon size equal to the spatial discretization size is then equivalent to a central difference scheme, thus motivating an augmented method. With this discretization, the best that can be done is to match the dispersion of a finite difference technique, though it will be clear that including a larger horizon size impacts dispersion. First, the dispersion relation for a second order accurate in space and time FDM can be given by

$$\cos(\omega \Delta t) = \gamma^2 \cos(\beta \Delta x) - \gamma^2 + 1, \tag{24}$$

where $\gamma = v\Delta t/\Delta x$ is the Courant number, $v = \sqrt{E/\rho}$ is the wave speed, ω is the angular frequency and β is the wavenumber.

In 1D, the discretized peridynamic operator becomes a sum of central differences in all of the nodes within the horizon. The addition of these points results in a different dispersion relation for each value of the horizon size δ. For example, with a horizon size of $2\Delta x$ and a central difference discretization in time, we have

$$\cos(\omega \Delta t) = \frac{\gamma^2}{2}\left[\cos(\beta \Delta x) + \frac{1}{4}\cos(2\beta \Delta x)\right] - \frac{5}{8}\gamma^2 + 1, \tag{25}$$

and for a horizon size of $3\Delta x$ we have

$$\cos(\omega \Delta t) = \frac{2\gamma^2}{9}\cos(\beta \Delta x) + \frac{\gamma^2}{9}\cos(2\beta \Delta x) + \frac{\gamma^2}{27}\cos(3\beta \Delta x) - \frac{10}{27}\gamma^2 + 1, \tag{26}$$

As an example, Fig. 1 gives a comparison of the dispersion curves of FDM and peridynamics with two horizon sizes, $\delta = 2\Delta x$ and $\delta = 3\Delta x$ for $\Delta x = 1$ mm, $\Delta t = 10$ ns, $E = 65$ GPa, and $\rho = 2{,}235$ kg/m^3.

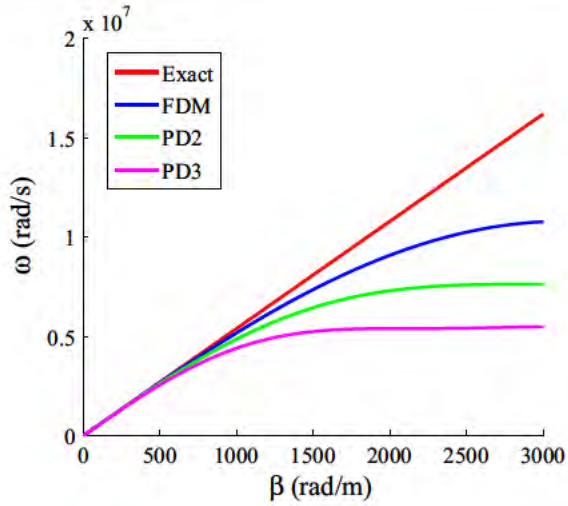

Fig. 1 Dispersion curves for FDM and discretized peridynamics with two horizon sizes

Again, as we wish to apply FDM to some areas of the computational domain, and peridynamics to others, these interfaces will exhibit frequency-dependent wave reflections because of the differing dispersion relations. The magnitude of these reflections will be investigated in Sect. 2.4.1.

2.4 Augmented method

The augmented method essentially implements a straight-forward FD discretization while simultaneously computing peridynamics-based bond strains as a fracture criterion. Unless fracture occurs, peridynamics is not used to compute internal forces, it is only used as a fracture criterion. After bond breakage occurs, peridynamics is then used to compute the internal forces.

2.4.1 Wave reflection at PD/FDM interfaces

As mentioned in Sect. 2.3 FDM exhibits numerical dispersion and peridynamics has inherent dispersion properties, which can be exacerbated when discretized. Our computational grid will contain areas that use both FDM and peridynamics to compute wave propagation, and so any interface between the two will result in reflections. The reflection coefficients can be computed based on the dispersion relations given in Eqs. (24), (25), and (26) using the numerical phase velocity. Here, we will simply give the relation in 1D, which would be

representative of a normally incident plane wave in an infinite medium. The reflection coefficient between two materials with different impedances is given by

$$\Gamma = \frac{Z_2 - Z_1}{Z_2 + Z_1}, \tag{27}$$

where Z_1 and Z_2 are impedances of the two media. In 1D, the acoustic impedance is given by

$$Z = \sqrt{E\rho} = \rho v. \tag{28}$$

If we use the phase velocity $v_\mathrm{p} = \omega/\beta$ and the dispersion relations from Eqs. 24, 25, and 26, we can substitute a numerical impedance into Eq. (27), resulting in

$$\Gamma_{\mathrm{PD2}} = \frac{\omega_{\mathrm{PD2}} - \omega_{\mathrm{FDM}}}{\omega_{\mathrm{PD2}} + \omega_{\mathrm{FDM}}}, \tag{29}$$

where

$$\omega_{\mathrm{FDM}} = \cos^{-1}\left\{\Delta t^{-1}\left[\gamma^2\cos(\beta\Delta x) - \gamma^2 + 1\right]\right\} \tag{30}$$

and

$$\omega_{\mathrm{PD2}} = \cos^{-1}\left\{\Delta t^{-1}\left[\frac{\gamma^2}{2}\left[\cos(\beta\Delta x) + \frac{1}{4}\cos(2\beta\Delta x)\right] - \frac{5}{8}\gamma^2 + 1\right]\right\}. \tag{31}$$

Similar results follow for other combinations of dispersion relations, three of which are plotted in Fig. 2 using the same parameters as those in Fig. 1. As expected, the wave reflection between computational grids becomes worse with increasing wavenumber and horizon size; however, this is only an illustrative example as in 2D and 3D the reflection coefficient will differ for angle of incidence and wave type (longitudinal vs. shear). We do of course expect similar behavior in general: Higher reflection coefficients for higher wavenumbers (or frequencies). Finally, while larger horizon sizes result in larger reflections between the FD/peridynamics interfaces, it has been observed that larger horizons yield more accurate crack features (Ha and Bobaru 2011). Ultimately, a large enough horizon should be used to model fracture, though continually increasing the horizon will result in less accurate behavior at computational interfaces. Consequently, in the dynamic fracture results (Sect. 3.4) a horizon of $3\Delta x$ will be used.

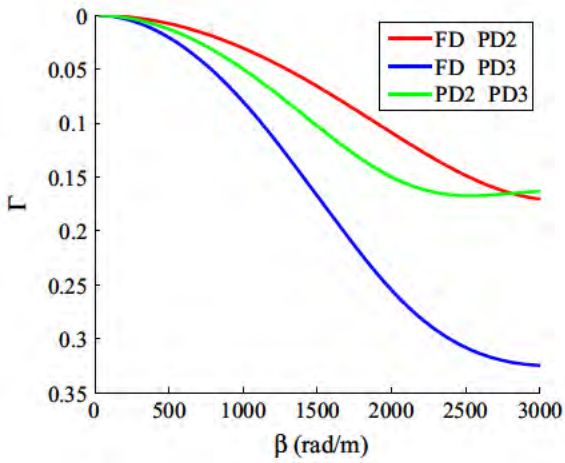

Fig. 2 Reflection coefficients for normal incidence between FDM and discretized peridynamic computational grids

2.4.2 Methodology

The augmented method proceeds as follows: The set of nodes is split into two sets, nodes at which internal forces are computed using finite differences N_{FD} and those at which internal forces are computed using peridynamics N_{PD}. These node sets do not overlap ($N_{\mathrm{FD}} \cap N_{\mathrm{PD}} = \emptyset$) and together they comprise the set of all nodes N ($N_{\mathrm{FD}} \cup N_{\mathrm{PD}} = N$). At each node, $\mathbf{r}_m \in N_{\mathrm{FD}}$, both the finite difference approximation of the internal force (divergence of the stress) and the peridynamic bond strains are computed, restated here as:

$$\mathbf{F}_m = \left[\begin{array}{l} \frac{2}{5}E\left(3\frac{\partial^2}{\partial x^2}u_\mathrm{x} + 2\frac{\partial^2}{\partial x\partial y}u_\mathrm{y} + \frac{\partial^2}{\partial y^2}u_\mathrm{x}\right) \\ \frac{2}{5}E\left(3\frac{\partial^2}{\partial y^2}u_\mathrm{y} + 2\frac{\partial^2}{\partial x\partial y}u_\mathrm{x} + \frac{\partial^2}{\partial x^2}u_\mathrm{y}\right) \end{array}\right]_{\mathbf{r}=\mathbf{r}_m}, \tag{32}$$

where u_x and u_y are functions of $\mathbf{r}$ and t, and with the appropriate finite differences applied to each differential operator. Simultaneously, at each node in N_{FD} the peridynamic bond strain is computed as given in Eq. (8), though it is not included in the internal force estimation until the failure criterion is met (see Eq. 9). After some bond strain s_{mn} exceeds the failure criterion, the internal force estimation switches to peridynamics, again given as

$$\mathbf{F}_m = \sum_{n=1}^{N_m} c\frac{\boldsymbol{\xi}_{mn}\otimes\boldsymbol{\xi}_{mn}}{|\boldsymbol{\xi}_{mn}|^3}\eta_{mn}V_{mn}, \tag{33}$$

thus moving the node from the set N_{FD} to the set N_{PD}.

In this way, peridynamics is used similar to cohesive zones in finite element methods: After some field

measure exceeds a critical value, a new constitutive response is used to model the internal force computation giving progressive failure/fracture modeling. In this way, the finite difference force computation can more accurately model the wave propagation in the bulk, and peridynamics can be used in damaged areas. This approach is summarized in Algorithm 1.

Data: $E, \rho, \delta, \Delta x, \Delta y, s_{\max}$
Result: **u**
compute integration weights at each node for peridynamic horizon, δ;
compute finite difference coefficients;
for *each time step* **do**
  for *each node m in* N_{FD} **do**
    compute force $\mathbf{F}_m$ using finite differences;
    compute bond strains, s_{mn};
    if *any* $s_{mn} > s_{\max}$ **then**
      break bond $\{m, n\}$;
      switch node m to peridynamics force computation;
    end
  end
  for *each node m in* N_{PD} **do**
    compute force $\mathbf{F}_m$ using peridynamics;
    compute bond strains, s_{mn};
    if *any* $s_{mn} > s_{\max}$ **then**
      break bond $\{m, n\}$;
    end
  end
  velocity Verlet temporal integration to update **u**;
  apply boundary conditions to **u**;
end

Algorithm 1: FDM augmented peridynamics method

2.4.3 Boundary conditions

Boundary conditions can be handled using either method, peridynamics or finite differences. Dirichlet boundary conditions are straightforward in either method. A traction-free, Neumann-like boundary condition in peridynamics is straightforward, and is implemented by excluding bonds in a horizon. In other words, a traction-free boundary conditions is set up when bonds are broken along a fracture. In the finite difference domain, the Neumann condition can be set by expanding the traction as a finite difference of boundary and internal nodes, and solving for the unknown boundary displacements in terms of the known internal displacements. For example, on a rectangular domain aligned with the Cartesian axis, the traction-free boundary condition on the top edge can be stated as

$$\hat{\mathbf{y}} \cdot \overline{\boldsymbol{\sigma}} = \mathbf{0}, \tag{34}$$

giving the coupled equations

$$\begin{aligned} \frac{\partial}{\partial y} u_{\text{x}} + \frac{\partial}{\partial x} u_{\text{y}} &= 0, \\ \frac{\partial}{\partial x} u_{\text{x}} + 3 \frac{\partial}{\partial y} u_{\text{y}} &= 0, \end{aligned} \tag{35}$$

where the factor of 3 in the second equation is a result of the constitutive relation of Eq. (16). Applying finite differences to the above, the unknown displacements on the boundary can be written in terms of known internal displacements as

$$\begin{aligned} &\Delta y u_{\text{y}}(x + \Delta x, y) - \Delta y u_{\text{y}}(x - \Delta x, y) \\ &\quad + 2\Delta x u_{\text{x}}(x, y) = 2\Delta x u_{\text{x}}(x, y - \Delta y), \\ &\Delta y u_{\text{x}}(x + \Delta x, y) - \Delta y u_{\text{x}}(x - \Delta x, y) \\ &\quad + 6\Delta x u_{\text{y}}(x, y) = 6\Delta x u_{\text{y}}(x, y - \Delta y), \end{aligned} \tag{36}$$

where a central difference has been used for the x derivative and a backward difference has been used for the y derivative. A sparse matrix can be formed to solve for the displacement at all boundary nodes after the displacement update in Eq. (7) is used to compute the internal displacements. Of course, in Eq. (35), the zeros on the right hand sides can be replaced with a loading function, taking care to include Young's modulus and the correct scaling factor for either plane strain or plane stress.

Unfortunately, it has been found that any interface between the finite difference method and peridynamics on a boundary can lead to high enough stress concentrations that spurious fracture can form. For now, the boundary of the material will be set to not accumulate damage other than pre-cracked regions.

3 Numerical results

In this section, several numerical results will be presented. The first will focus on comparing the dispersion effects of the finite difference discretization and discretized peridynamics. Next, reflections at the interface between the two computational regions will be demonstrated. In Sect. 3.3, the stress intensity factor of a semi-infinite line crack in an infinite medium will be compared in both the hybrid and peridynamic approaches. Finally, a dynamic fracture problem will be illustrated in Sect. 3.4.

3.1 Dispersion comparison

In this subsection, the dispersion effects of a finite difference method and discretized peridynamics with two horizons ($2\Delta x$ and $3\Delta x$) in a 2D plane strain setting are compared. The constitutive parameters are given by Young's modulus $E = 65$ GPa and density $\rho = 2{,}235\,\text{kg/m}^3$ and the discretization parameters are given by x-step of $\Delta x = 1$ mm, y-step of $\Delta y = 1$ mm, and time step size of $\Delta t = 10$ ns. Poisson's ratio is fixed at $\nu = 1/4$ as discussed above. The computational region is a 200 mm-by-200 mm^2 (spanning the region $0 \le x, y \le 200$ mm), chosen to be large enough so boundary effects do not influence the results. A plane wave with a Gaussian profile is used as an initial condition—so as to compare with an exact solution—given by

$$\mathbf{u}(\mathbf{r}, t = 0) = \exp\left[-7.5 \times 10^4 \left(\mathbf{r} \cdot \hat{\mathbf{x}} - 0.1\right)^2\right] \hat{\mathbf{x}}. \tag{37}$$

The simulation is run for 10 μs and u_x is observed at the points $\mathbf{r} = (70, 100)$ mm and $\mathbf{r} = (80, 100)$ mm.

First, Fig. 3 shows the x-directed displacement u_x vs. time at the two points listed above. The displacement measured at 80 mm is shown as the solid lines and the displacement at 70 mm is shown as the dashed lines. An "exact" solution (determined assuming a 1D problem, though the numerical solutions were computed in 2D) is shown as the red curves, the finite difference approximated solution is shown as the black curves, and two peridynamics approximated solutions are shown in green and blue, using horizons of $3\Delta x$ and $2\Delta x$ respectively. As can be seen, peridynamics with a higher horizon displays errors characteristic of dispersion effects, namely a lowered amplitude and oscillations. Next, the Fourier transform of the x-directed displacement was computed and is shown in Fig. 4, along with the absolute error in each solution compared with the "exact" solution (Fig. 5). These figures demonstrate that, compared to the finite difference approximation, higher frequencies in the peridynamics methods display larger errors, consistent with dispersion errors.

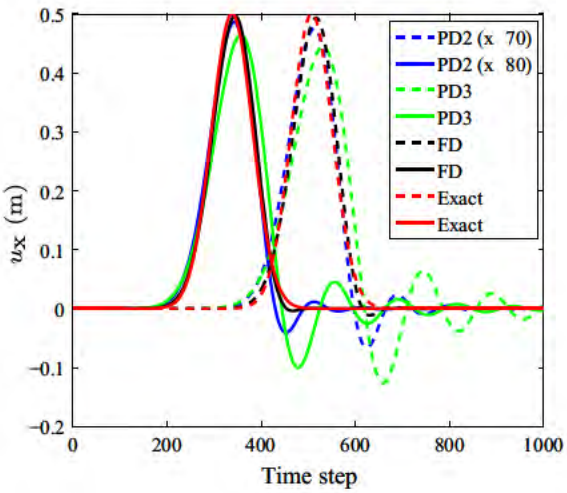

Fig. 3 The x-directed displacement versus time step measured at two points, demonstrating dispersion effects

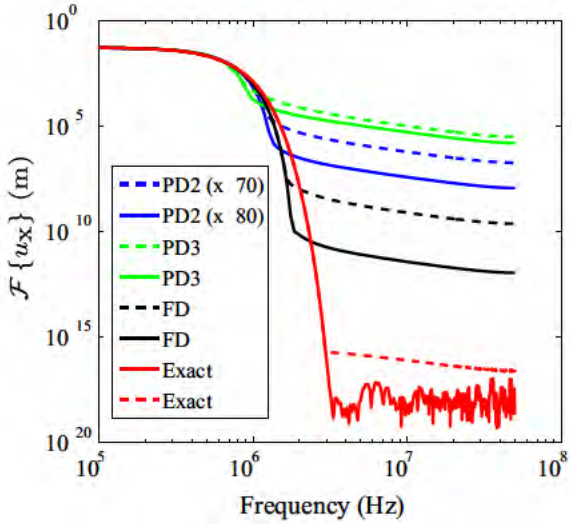

Fig. 4 Fourier transform of Fig. 3

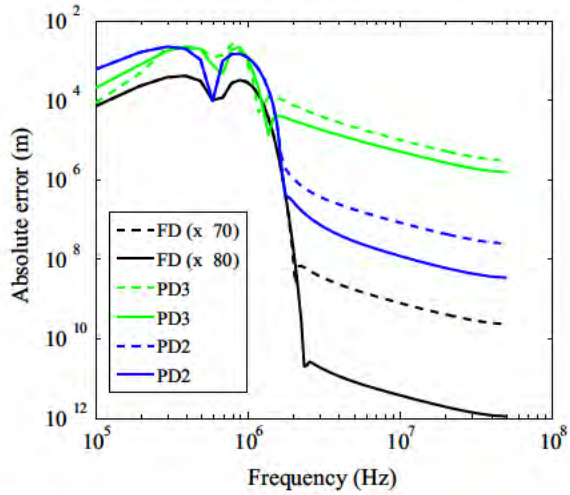

Fig. 5 Absolute error in the Fourier transform of Fig. 3 measured against the exact solution

3.2 Interface reflections

Wave reflections between computational regions are examined here. This was discussed in an analytical form for 1D in Sect. 2.4.1, though here we perform numerical tests of the 2D algorithms. In the first test, the parameters of the problem are identical to those of the previous subsection, though now the left half of the domain will be computed with the finite difference method and the right half will use peridynamics with a horizon size of either $3\Delta x$ or $2\Delta x$. The initial condition is again a Gaussian pulse, now centered at the line $x = 75$ mm and the x-directed displacement is now measured at the point $\mathbf{r} = (90, 100)$ mm.

As shown in Fig. 6, the reflected wave can be examined by also computing the solution to this problem with a fully finite difference domain, and subtracting the results, thus leaving only the reflected wave in the left half domain. In Fig. 6, the blue curve is the result using peridynamics with a horizon of $3\Delta x$ in the right-half and the red curve shows the simulation with a horizon of $2\Delta x$. Given that the magnitude of the incident pulse was 0.5 m, the reflections at the interface can be significant for the $3\Delta x$ horizon size. By maximum magnitude, the reflected wave is approximately 12%; however, peridynamics will only ever be used in regions that have experienced fracture or failure, so some amount of wave reflection would be expected regardless.

Given the above, it may however also be possible that the anomalies seen in Fig. 6 may be due to the

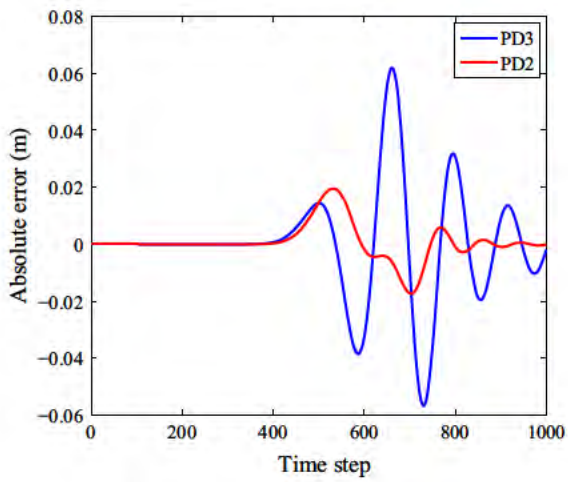

Fig. 6 Absolute error between a fully FD solution and a solution with half peridynamics, half FD

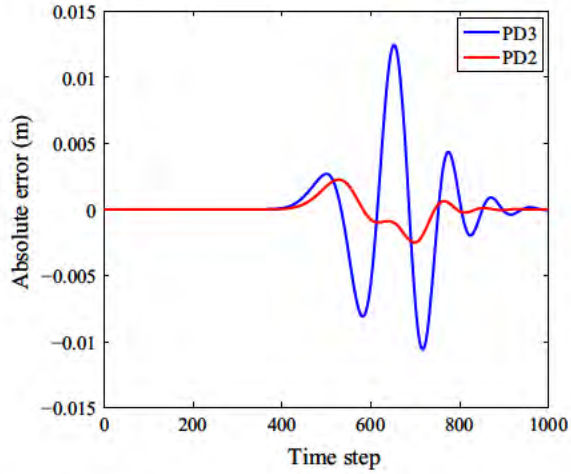

Fig. 7 Absolute error between a fully FD solution and a solution with a *vertical line* of peridynamic nodes

dispersion properties of the peridynamic region. To test this, we again perform the above simulation in a FD domain with peridynamics "window" consisting of a single vertical line of nodes at the line $x = 100$ mm. The smaller window will reduce the dispersion effects of a wave propagating through a peridynamic region, but still demonstrate the effects of interface reflection. Figure 7 gives the results of this test, with the blue curve showing peridynamics with a horizon of $3\Delta x$ and the red curve having a horizon of $2\Delta x$.

For a fully fractured region, a free surface is formed and 100% of a wave is reflected, so as a final test, we introduce a free surface with boundary conditions implemented using finite differences to compare a fracture surrounded by peridynamic nodes. The same set up is used as described above, though here the free surface is placed at $x = 100$ mm. The initial pulse is centered at the line $x = 70$ mm and the result shown in Fig. 8 is measured at the point $\mathbf{r} = (90, 100)$ mm. Again, Fig. 8 shows the difference between the fully FD simulation and the simulation using a peridynamic boundary with a thickness of one horizon.

3.3 Stress intensity comparison

Next, the augmented method and peridynamics are compared using the dynamic mode I stress intensity factor at a semi-infinite, stationary crack in an infinite medium. This problem has an analytical solution for the stress intensity factor for both stationary and

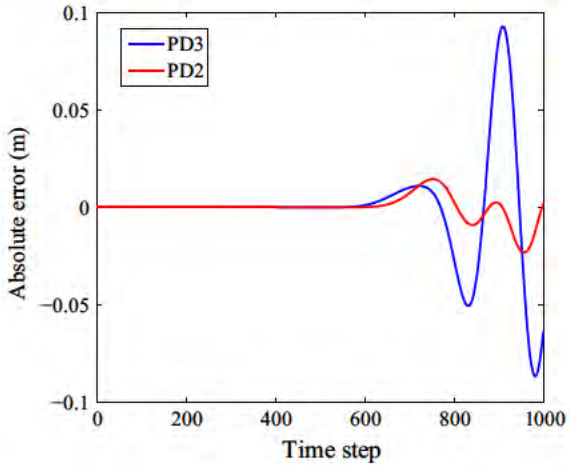

Fig. 8 Absolute error between a fully FD solution and a solution with a peridynamic border

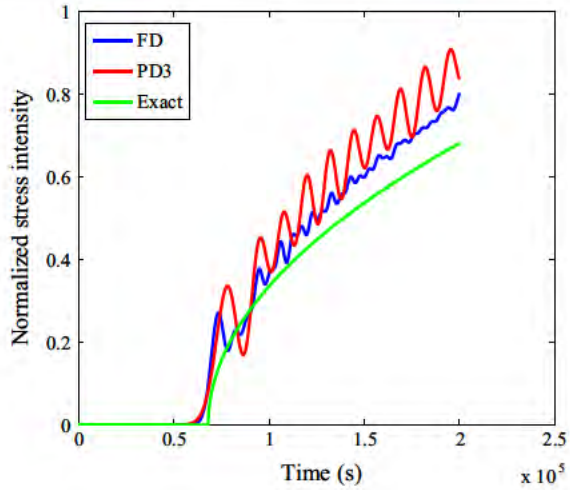

Fig. 9 Normalized stress intensity factor comparison between hybrid and peridynamics

moving cracks (Liu et al. 2011), though here we focus on the stationary case. As given by Liu et al. (2011), the stress intensity factor for this geometry can be stated as

$$K_{\mathrm{I}}(t) = H(t - t_{\mathrm{c}}) \frac{2\sigma^*}{1-\nu} \sqrt{\frac{v_{\mathrm{l}}(t - t_{\mathrm{c}})(1-2\nu)}{\pi}}, \tag{38}$$

where $H(\cdot)$ is the Heaviside step function, v_{l} is the longitudinal wave speed, and σ^* is the applied stress. To simulate an infinite problem, a large region is used with a horizontal pre-crack through the center and the simulation is stopped before the reflected wave reaches the crack tip. The material properties used give a longitudinal wave speed of $v_{\mathrm{l}} = 7{,}332$ m/s with Poisson's ratio 1/4. Finally, the applied tensile stress is 40 MPa.

To estimate the stress intensity factor in the simulation, the method outlined by Chen (1975) will be used. To summarize, the stress at the crack tip can be expressed

$$\sigma_{\mathrm{yy}} \approx \frac{K_{\mathrm{I}}^*(t)}{\sqrt{2\pi r}} \left(1 + \sin\frac{\theta}{2}\sin\frac{3\theta}{2}\right)\cos\frac{\theta}{2}, \tag{39}$$

where $K_{\mathrm{I}}^*(t)$ is a low-order estimate of the stress intensity, r is the distance to the crack tip, and θ is the angle. The stress intensity factor $K_{\mathrm{I}}(t)$ can then be estimated by choosing nodes along a line with constant angle with respect to the crack tip, computing the stress at those points using finite differences, and constructing a least squares approximation of the stress near the crack tip. More precisely, we choose nodes along the line $\theta = 0$ (typically five nodes, starting with the fourth closest to the crack tip) and use the higher order approximation of the stress intensity

$$K_{\mathrm{I}}^* \approx K_{\mathrm{I}} + \alpha(\theta) r^{1/2} + \beta(\theta) r + \gamma(\theta) r^{3/2}, \tag{40}$$

and, according to Chen (1975), the coefficients of non-integer powers of r, $\alpha(\theta)$ and $\gamma(\theta)$, are zero for $\theta = 0$. A least squares approximation is then used to estimate $K_{\mathrm{I}}(t)$ (Chen 1975). Figure 9 shows the normalized stress intensity factor (normalized by $\sigma\sqrt{\pi a}$ where $a = 150$ mm is the crack length) with the exact solution and both peridynamics and the hybridized method. The oscillations seen in peridynamics (most likely due to wave dispersion) are reduced in the hybrid method.

3.4 Dynamic fracture

Finally, a dynamic crack propagation problem is simulated. The problem setup is that described in (Kalthoff 1974): A 150 mm horizontal crack in a 300 mm-by-100 mm-by-9 mm glass plate is propagated with a tensile load of 3,040 N. No material properties are given in (Kalthoff 1974), so we use properties given in (Ha and Bobaru 2010) for soda-lime glass: Young's modulus of 72 GPa, density of 2,440 kg/m^3, and Poisson ratio of 1/3 (restricted for plane stress). We also have chosen a fracture energy value of 3 J/m^2, which gives a crack pattern that most closely matches the experiment in (Kalthoff 1974). While this fracture energy

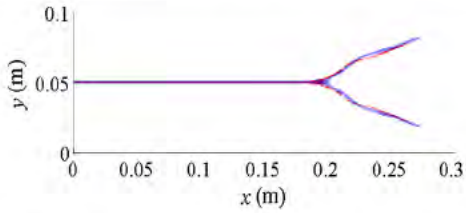

Fig. 10 Comparison of crack paths between the hybrid method (*red*) and peridynamics (*blue*)

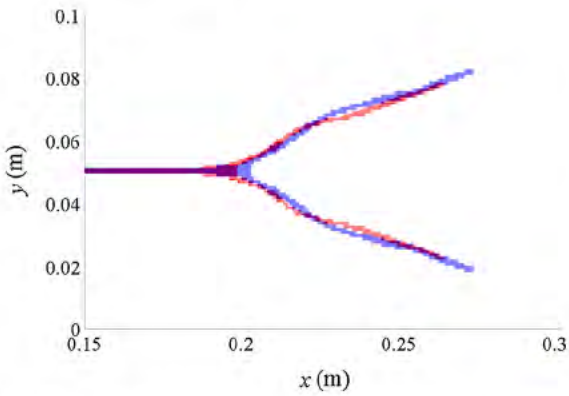

Fig. 11 Magnification of the crack branching area of Fig. 10

appears somewhat low, it is close to the value of approximately 8 J/m^2 found in the literature for crack initiation (Döll 1975). Finally, in the peridynamics simulations, the load is applied as a body force as described in Ha and Bobaru (2009), and as a traction boundary condition in the hybrid method, with a traction of 1.13 MPa.

First, discretization sizes of $\Delta x = 1$ mm, $\Delta y = 1$ mm, and $\Delta t = 10$ ns were used in both methods and the simulations were run for 100 μs (10,000 time steps) with a horizon size of $\delta = 3\Delta x$. The final crack patterns are shown in Fig. 10, where a crack is taken to be any node with damage >0.4 (as measured by the ratio of the number of broken bonds to the number of initial bonds) and the hybrid result is shown in red and the peridynamics is shown in blue. Figure 11 shows a magnified view of the crack branch: As can be seen, both methods branch at approximately the same location, though they differ somewhat in their subsequent crack paths.

The same problem was repeated, though now with discretization sizes of $\Delta x = 0.5$ mm and $\Delta y = 0.5$ mm, and with a horizon again of $\delta = 3\Delta x$. Figure 12 shows the results of the simulations, again with the hybrid method in red and the peridynamics in blue. Here, the

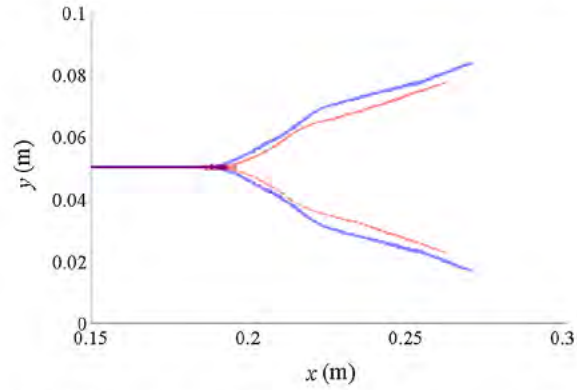

Fig. 12 Magnification of the crack branching area with a finer discretization

peridynamic method alone appears to have an earlier crack initiation time. This is investigated further by tracking the crack tip position and speed versus time.

The crack speeds were estimated (for the finer discretization) by tracking the damage as it propagated across the domain and are shown in Fig. 13. The location of the crack was recorded at every 5 μs (500 time steps) (shown in Fig. 14) and the crack speed was estimated by computing the central difference of the result. The hybrid method has a crack initiation time slightly later than the peridynamics results and a crack speed slightly slower than that of the peridynamics. These differences are most likely due to the lower stress intensity factor observed (see Fig. 9) at the crack tip of the hybrid method. This can be confirmed by comparing the end points of the cracks in Fig. 12. Two features can be seen in the crack speed data in the form of the two dips in crack speed around 35 and 65 μs. The first drop in speed occurs as the crack branches and the second when the branch angles change slightly at 225 mm.

It is also illustrative to compare both methods between the two discretizations given above. To that end, Fig. 15 shows the peridynamic method at both of the above discretizations. It can be seen in the figure that the crack initiation occurs slightly earlier in the finer discretization (shown in red). In contrast, the hybrid method shows a more stable fracture path, with both following a very similar path and initiation time (Fig. 16). In both figures, the coarse discretization is plotted in blue and the fine discretization is shown in red. These differences are most likely caused by the oscillations seen in the stress intensity factor, due to the higher dispersion in the peridynamic method alone.

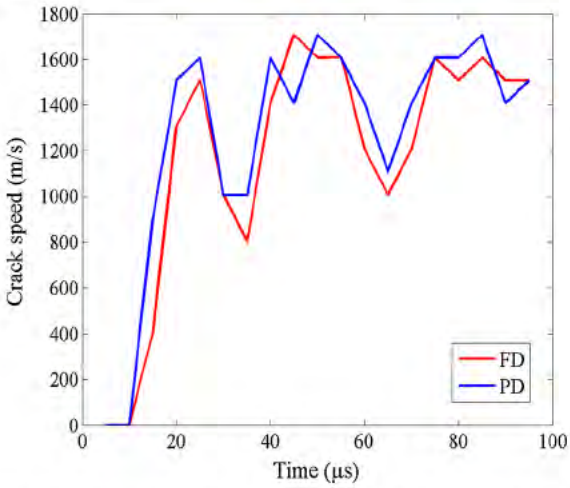

Fig. 13 Comparison of crack speeds of the hybrid method (*red*) and peridynamics (*blue*)

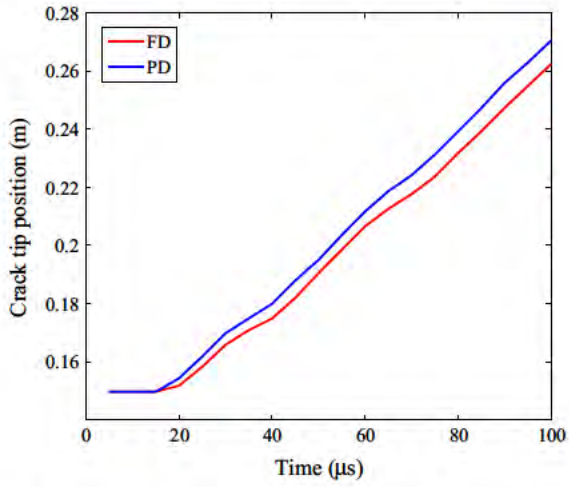

Fig. 14 Comparison of crack tip locations of the hybrid method (*red*) and peridynamics (*blue*)

Finally, the dynamic fracture problem was repeated with both discretizations used above, but with a higher load of 6080 N. In this case, a more complicated crack path is observed, with a larger difference between the methods. Figure 17 shows the result using discretization sizes of $\Delta x = 1$ mm, $\Delta y = 1$ mm. A major difference between the two methods is the shallower crack branch angle at the branch onset and the additional branch close to the center in the hybrid method. Otherwise, they both feature multiple branches, consistent with crack patterns seen at higher loads (Bowden et al. 1967; Ha and Bobaru 2011). Figure 18 shows

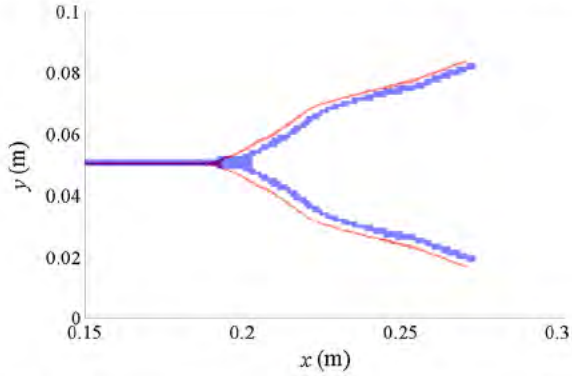

Fig. 15 Comparison of crack paths at different discretizations (coarse in *blue* and fine in *red*) using peridynamics

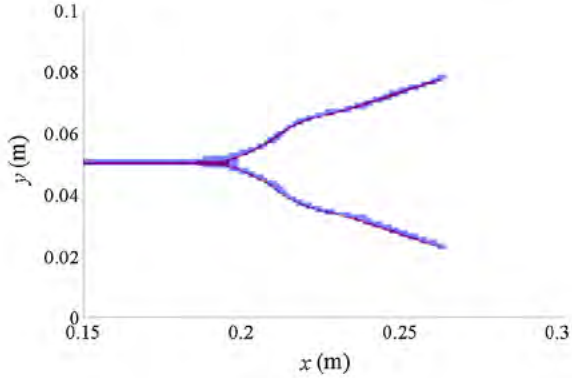

Fig. 16 Comparison of crack paths at different discretizations (coarse in *blue* and fine in *red*) using the hybrid method

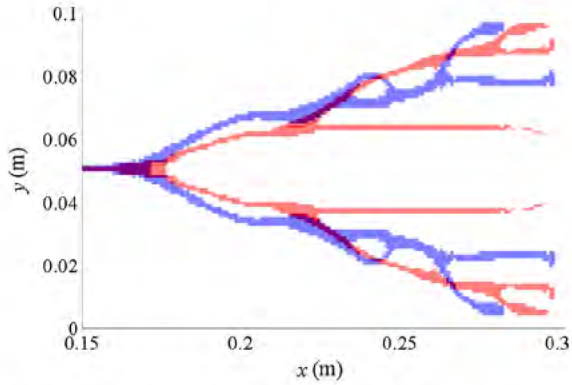

Fig. 17 Comparison of crack paths at a higher load and a coarse discretization

the result using discretization sizes of $\Delta x = 0.5$ mm, $\Delta y = 0.5$ mm. At this discretization, the peridynamics solution features an additional branch near the far edge and two arrested cracks not seen at the coarse discretization of the peridynamics method.

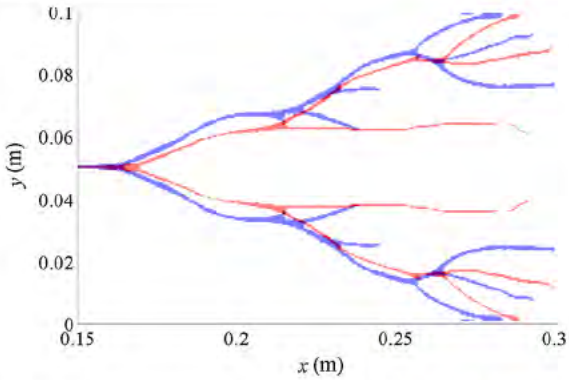

Fig. 18 Comparison of crack paths at a higher load and a fine discretization

4 Conclusions

A hybrid finite difference/peridynamics method was presented to improve the dispersion properties of stand-alone peridynamics. The hybrid method essentially switches the spatial internal force computation between finite differences (divergence of the stress) and peridynamics (integral of a micro-force function) after a damage criterion is met. Linearized peridynamics can be shown to model linear elastic materials with specific Poisson ratios, and this fact is used to develop a matching finite difference scheme. Analysis was presented showing the dispersion properties of discretized peridynamics in 1D in comparison to a straight-forward finite difference discretization. Numerical results were also shown to demonstrate the dispersion properties of the two methods in 2D. Other results show that the numerically-computed stress intensity factor for peridynamics can oscillate, which may lead to differing crack paths.

This method has a number of possible extensions, such as 3D, state-based peridynamics, and non-linear materials. Additional work may be done as well to ease the transition region between peridynamics and finite differences, as reflections can occur due to the differing material representations.

References

Alterman Z, Karal F (1968) Propagation of elastic waves in layered media by finite difference methods. Bull Seismol Soc Am 58(1):367–398

Azdoud Y, Han F, Lubineau G (2013) A morphing framework to couple non-local and local anisotropic continua. Int J Solids Struct 50(9):1332–1341

Azdoud Y, Han F, Lubineau G (2014) The morphing method as a flexible tool for adaptive local/non-local simulation of static fracture. Comput Mech 54:1–12

Bobaru F, Duangpanya M (2010) The peridynamic formulation for transient heat conduction. Int J Heat Mass Transf 53(19–20):4047–4059

Bobaru F, Ha YD (2011) Adaptive refinement and multiscale modeling in 2D peridynamics. Int J Multiscale Comput Eng 9(6):635–659

Bobaru F, Yang M, Alves LF, Silling SA, Askari E, Xu J (2009) Convergence, adaptive refinement, and scaling in 1D peridynamics. Int J Numer Method Biomed Eng 77(6):852–877

Bowden FP, Brunton JH, Field JE, Heyes AD (1967) Controlled fracture of brittle solids and interruption of electrical current. Nature 216:38–42

Brian PLT (1961) A finite-difference method of high-order accuracy for the solution of three-dimensional transient heat conduction problems. AIChE J 7(3):367–370

Chen YM (1975) Numerical computation of dynamic stress intensity factors by a lagrangian finite-difference method (the hemp code). Eng Fract Mech 7(4):653–660

Courant R, Friedrichs K, Lewy H (1928) Über die partiellen Differenzengleichungen der mathematischen Physik. Math Ann 100:32–74

Döll W (1975) Investigations of the crack branching energy. Int J Fract 11:184–186

Emmrich E, Weckner O (2006) The peridynamic model in nonlocal elasticity theory. Proc Appl Math Mech 6:155–156

Foster JT, Silling SA, Chen WW (2010) Viscoplasticity using peridynamics. Int J Numer Methods Eng 81(10):1242–1258

Gerstle W, Silling S, Read D, Tewary V, Lehoucq R (2008) Peridynamic simulation of electromigration. Science 8(2):75–92

Ha YD, Bobaru F (2009) Traction boundary conditions in peridynamics: a convergence study. Tech rep, University of Nebraska-Lincoln

Ha YD, Bobaru F (2010) Studies of dynamic crack propagation and crack branching with peridynamics. Int J Fract 162(1–2):229–244

Ha YD, Bobaru F (2011) Characteristics of dynamic brittle fracture captured with peridynamics. Eng Fract Mech 78(6):1156–1168

Hesthaven JS, Warburton T (2002) Nodal high-order methods on unstructured grids: I. Time-domain solution of Maxwell's equations. J Comput Phys 181(1):186–221

Kalthoff JF (1974) On the propagation direction of bifurcated cracks. In: Sih GC (ed) Dynamic crack propagation. Springer, Dordrecht, pp 449–458

Liu ZL, Menouillard T, Belytschko T (2011) An XFEM/Spectral element method for dynamic crack propagation. Int J Fract 169(2):183–198

Lubineau G, Azdoud Y, Han F, Rey C, Askari A (2012) A morphing strategy to couple non-local to local continuum mechanics. J Mech Phys Solids 60(6):1088–1102

Mikata Y (2012) Analytical solutions of peristatic and peridynamic problems for a 1d infinite rod. Int J Solids Struct 49(21):2887–2897

Seleson P, Beneddine S, Prudhomme S (2013) A force-based coupling scheme for peridynamics and classical elasticity. Comput Mater Sci 66:34–49

Silling S (2000) Reformulation of elasticity theory for discontinuities and long-range forces. J Mech Phys Solids 48(1):175–209

Silling S, Askari E (2005) A meshfree method based on the peridynamic model of solid mechanics. Comput Struct 83(17–18):1526–1535

Silling SA, Epton M, Weckner O, Xu J, Askari E (2007) Peridynamic states and constitutive modeling. J Elast 88(2): 151–184

Taflove A, Brodwin ME (1975) Numerical solution of steady–state electromagnetic scattering problems using the time-dependent Maxwell's equations. IEEE Trans Microw Theory Tech 23:623–630

Virieux J (1986) P-sv wave propagation in heterogeneous media: velocitystress finite difference method. Geophysics 51(4):889–901

Weckner O, Abeyaratne R (2005) The effect of long-range forces on the dynamics of a bar. J Mech Phys Solids 53(3):705–728

Wildman RA, Gazonas GA (2013) A perfectly matched layer for peridynamics in two dimensions. J Mech Mater Struct 7(8):765–781

Yee K (1966) Numerical solution of initial boundary value problems involving Maxwell's equations in isotropic media. IEEE Trans Antennas Propag 14(3):302–307

Zahradnik J, Hron F (1992) Robust finite-difference scheme for elastic waves on coarse grids. Studia Geophysica et Geodaetica 36(1):1–19

1 (PDF) DEFENSE TECH INFO CTR
DTIC OCA

2 (PDF) US ARMY RSRCH LAB
IMAL HRA MAIL & RECORDS MGMT
RDRL CIO LL TECHL LIB

1 (PDF) GOVT PRNTG OFC
A MALHOTRA

52 (PDF) US ARMY RSRCH LAB
RDRL CIH
J KNAP
RDRL WM
B FORCH
S KARNA
J MCCAULEY
RDRL WML B
I BATYREV
J BRENNAN
E BYRD
S IZVYEKOV
W D MATTSON
B RICE
D TAYLOR
N WEINGARTEN
RDRL WML H
C MEYER
B SCHUSTER
RDRL WMM
J BEATTY
R DOWDING
J ZABINSKI
RDRL WMM B
T BOGETTI
C FOUNTZOULAS
G GAZONAS
D HOPKINS
B LOVE
B M POWERS
T WALTER
R WILDMAN
C YEN
J YU
RDRL WMM D
S WALSH
RDRL WMM E
J LASALVIA
RDRL WMM F
M TSCHOPP
RDRL WMM G
J ANDZELM
T CHANTAWANSRI
C RINDERSPACHER
T SIRK
Y SLIOZBERG
RDRL WMP
S E SCHOENFELD
RDRL WMP B
S SATAPATHY
A SOKOLOW
T WEERASOORIYA
RDRL WMP C
D CASEM
A TONGE
B LEAVY
C WILLIAMS
J CLAYTON
J LLOYD
M GREENFIELD
S BILYK
S SEGLETES
T W BJERKE
D DANDEKAR
RDRL WMP D
R DONEY
C RANDOW

INTENTIONALLY LEFT BLANK.